Applied Catalysis A: General 477 (2014) 54–63

Contents lists available at ScienceDirect

Applied Catalysis A: General

journal homepage: www.elsevier.com/locate/apcata

# Preferential CO oxidation (CO-PROX) catalyzed by CuO supported on nanocrystalline $CeO_2$ prepared by a freeze-drying method

Ana Arango-Díaz[a], Elisa Moretti[b], Aldo Talon[b], Loretta Storaro[b], Maurizio Lenarda[b], Pedro Núñez[c], Jaasiel Marrero-Jerez[c], José Jiménez-Jiménez[a], Antonio Jiménez-López[a], Enrique Rodríguez-Castellón[a,*]

[a] Departamento de Química Inorgánica, Cristalografía y Mineralogía, Facultad de Ciencias, Universidad de Málaga, Campus de Teatinos, 29071 Málaga, Spain
[b] Dipartimento di Scienze Molecolari e Nanosistemi, Università Ca' Foscari Venezia, Via Torino 155/b, 30172 Mestre-Venezia, Italy
[c] Departamento de Química Inorgánica, Universidad de La Laguna, La Laguna, Tenerife, Spain

ARTICLE INFO

*Article history:*
Received 11 December 2013
Received in revised form 1 February 2014
Accepted 19 February 2014
Available online 3 March 2014

*Keywords:*
$CeO_2$ nanocrystalline
Freeze-drying method
Copper oxide
Preferential CO oxidation
Hydrogen

ABSTRACT

Nanocrystalline $CeO_2$ with a regular size of 9.5 nm was prepared by a freeze-drying method, and subsequent impregnated with a Cu(II) acetate solution, varying the loading of Cu (3, 6, 12 wt.%). The resulting $CuO/CeO_2$ materials were characterized by $N_2$ physisorption at −196 °C, HRTEM, $H_2$-TPR, X-ray diffraction, Raman spectroscopy and XPS and tested as catalysts in the preferential CO oxidation in a $H_2$-rich stream (CO-PROX) in the temperature range 40–190 °C. In spite of their low specific surface areas the catalysts exhibited a good catalytic performance, resulting active and selective in the CO-PROX reaction at low temperatures. The inhibiting effect of the simultaneous presence of $CO_2$ (15 vol.%) and $H_2O$ (10 vol.%) in the reaction mixture on the performance of $CuO-CeO_2$ catalysts was also investigated. The addition of $CO_2$ and water in the gas stream depressed CO oxidation up to 160 °C, its effect being negligible at higher temperatures. Nevertheless, despite these expected deactivation phenomena, a CO conversion value higher than 90% and a $CO_2$ selectivity of about 90% was achieved for all the samples at 160 °C. The excellent performance, especially shown by the catalyst with 6 wt%. of copper, has been related to the wide dispersion of the copper active sites associated with the high amount of $Ce^{4+}$ species before reaction.



## 1. Introduction

In the new energy scenario, fuel cells have emerged as one of the most important power generation systems. Among the different types of fuel cells, particularly, the Polymer Exchange Membrane Fuel Cells (PEMFCs) have been intensively studied during the last few years as a result of the increasing interest on the development of more efficient, and environmentally friendly, ways of energy generation [1,2].

Hydrogen-rich gas streams production mainly uses steam reforming of hydrocarbons followed by the water gas shift reaction. The resulting gas mixtures contain about 1% CO, but the CO concentration has to be reduced below 10 ppm, if the stream is used to feed a PEMFC, because the Pt anode is highly sensitive to CO poisoning [3]. One of the most straightforward and cost effective methods for the elimination of CO is the preferential catalytic oxidation (CO-PROX) [4–6]. The catalysts for CO-PROX must be highly selective in a wide temperature range, tolerant to $CO_2$ and $H_2O$, and stable for long time. One of the most investigated alternatives to noble metal catalytic systems for CO-PROX is CuO supported on $CeO_2$. $CuO-CeO_2$ based systems appear to be selective, thermally stable and cheaper than other classes of catalysts [7–11].

Their performances are mainly attributed to the synergistic redox properties of the copper–ceria interfacial sites [12–18]. In the preferential oxidation of carbon monoxide, the presence of oxygen vacancy defects (OVDs) and other lattice defects can play a very important role in the surface reactivity [18]. The high performance of copper-ceria catalysts can be, in this sense, ascribed to the strong interaction between the active phase and the support, favored by the elevated concentration of structural defects in cerium oxide [19–21]. Zheng et al. confirmed that the catalytic activity was governed both by the $Cu^+/Cu^{2+}$ and $Ce^{3+}/Ce^{4+}$ redox couples [22]. In addition, several authors [23–26] concluded that the CuO species in both fully oxidized and partially reduced states were significantly

* Corresponding author. Tel.: +34 952131873; fax: +34 952131870.
*E-mail address:* castellon@uma.es (E. Rodríguez-Castellón).

http://dx.doi.org/10.1016/j.apcata.2014.02.033
0926-860X/

affected by the interaction with underlying $CeO_2$ support and the degree of promotion of such reduction could be also affected by modifying the nature of the support, because the catalytic properties can be strongly affected by the synthethic methodology used [7,27].

A new promising synthesis method used to prepare ceria-based systems containing gadolinium and samarium [28,29], was applied to prepare a pure ceria solid by a freeze-drying method able to yield nanocrystalline materials [30], allowing to achieve much higher dense pellets.

As known, freeze-drying is a process which consists on removing water from a frozen sample by sublimation and desorption under vacuum. Nevertheless, this process generates various stresses during freezing and drying steps. So, protectants are usually added to the formulation to protect the nanoparticles from freezing and desiccation stresses. This methodology has been exploited for preparing various porous materials, including organic [31], inorganic [32,33] and composite materials [34].

In this paper, we describe the preparation of a nanocrystalline $CeO_2$ by a simple freeze-drying method and its subsequent impregnation with a copper(II) acetate solution, by varying the loading of Cu (3, 6, 12 wt.%). The obtained materials were fully characterized and studied as catalysts to selectively oxide CO to $CO_2$ in the presence of excess hydrogen in the temperature range 40–190 °C.

## 2. Experimental

### 2.1. Sample preparation

#### 2.1.1. $CeO_2$ preparation

$CeO_2$ polycrystalline powders were synthesized by a freeze-drying method, using $Ce(NO_3)_3{\cdot}6H_2O$ (99.9%, Aldrich) as precursor. Cerium(III) nitrate was dissolved in distilled water and then ethylenediaminetetraacetic acid (EDTA) (99.7% Aldrich) was added as complexing agent to prevent precipitation in a 1:1 molar ligand:metal ratio. The pH of the solution was initially acid so it was adjusted at 7–8 by adding aqueous ammonia. The solution was flash frozen dropwise into liquid nitrogen and then dried in a Heto Lyolab freeze-dryer equipment for 3 days. The obtained amorphous precursor was immediately calcined at 300 °C for 2 h to prevent rehydration and to eliminate the organic matter by combustion. Finally, the powder was calcined in an alumina crucible at 600 °C for 5 h. Under these synthesis conditions, crystallization of $CeO_2$ powders to a single phase was achieved [30]. The sample was labeled $CEO_2$.

#### 2.1.2. $CuO$-$CeO_2$ catalysts preparation

The active phase was added by incipient wetness impregnation of the ceria using a copper(II) acetate monohydrated (Aldrich) solution with the adequate concentration to get a nominal copper loading of 3.0, 6.0 and 12.0 wt.%. After impregnation the materials were dried overnight at 60 °C and calcined during 4 h at 400 °C. The catalysts were named *x*CUCE, with $x = 3$, 6 and 12, referring to the Cu (wt.%) present in the samples.

### 2.2. Catalytic tests

Catalytic activity tests were carried out in a laboratory flow apparatus, with a fixed bed reactor operating at atmospheric pressure. The catalysts (0.100 g), with a defined particle size (0.050–0.110 mm) were introduced into a tubular Pyrex glass reactor (5 mm i.d.), and placed inside an aluminum heating block. Before the catalytic experiments, the samples were heated in situ at 400 °C under flowing air for 30 min, followed by cooling to RT in He flow. The contact time W/F was 0.18 g s $cm^{-3}$ (GHSV = 22,000 $h^{-1}$). The reaction mixture composition was 1.2% CO, 1.2% $O_2$, 50% $H_2$, balanced with He. The effect of $CO_2$ and $H_2O$ was examined in separate runs with the addition of 15 vol.% $CO_2$ and 10 vol.% $H_2O$. An ice-cooled cold finger was used to trap the excess of water downstream from the reactor. A HP6890CG gas chromatograph equipped with a thermal conductivity detector (TCD) was used to analyze the outlet composition. A CP Carboplot P7 column was used, with helium as carrier. The temperature was varied in the 40–190 °C range, and measurements were carried out till a steady state was achieved. Both methanation and reverse water-gas-shift reactions were found to be negligible in our experimental conditions. The carbon monoxide (the detection limit for CO was 10 ppm) and oxygen conversions were calculated based on the CO (Eq. (1)) and $O_2$ (Eq. (2)) consumption, respectively:

$$x_{CO}(\%) = \frac{n_{CO}^{in} - n_{CO}^{out}}{n_{CO}^{in}} \times 100 \quad (1)$$

$$x_{O_2}(\%) = \frac{n_{O_2}^{in} - n_{O_2}^{out}}{n_{O_2}^{in}} \times 100 \quad (2)$$

The selectivity towards $CO_2$ was calculated by (Eq. (3)):

$$sel_{CO_2}(\%) = \frac{1}{\lambda}\frac{x_{CO}}{x_{O_2}} \times 100 \quad (3)$$

and the excess of oxygen factor ($\lambda$) is defined as (Eq. (4)):

$$\lambda = 2 \times \frac{n_{O_2}^{in}}{n_{CO}^{in}} \quad (4)$$

In all the catalytic tests, $\lambda = 2$ was used, because this value was previously found optimal for preferential oxidation of CO [10–12].

### 2.3. Characterization methods

$N_2$ adsorption–desorption measurements were performed at liquid nitrogen temperature (−196 °C) with an ASAP 2020 apparatus from Micromeritics. Before each measurement, samples were outgassed 12 h at 200 °C and $1 \times 10^{-2}$ Pa. The specific surface area ($S_{BET}$) was calculated using the BET equation, and the specific pore volume ($V_p$) was calculated at $P/P_0 = 0.98$. The pore size distribution was calculated following BJH method, taking the data of the adsorption branch and assuming a cylindrical pore model.

Transmission Electron Microscopy (TEM) images were taken on a JEOL-JEM 3010 high-resolution microscope (point resolution at Scherzer defocus 0.17 nm), equipped with a lanthanum hexaboride (LaB6) gun, using an accelerating voltage of 300 kV. The images were taken with a CCD camera (Gatan, mod. 694). The powder was suspended in isopropyl alcohol and dropped on a holey carbon film grid.

Hydrogen temperature-programmed reduction ($H_2$-TPR) experiments were carried out using 0.08 g of freshly calcined catalyst placed in U shaped quartz reactor inside of a tubular oven. In order to remove contaminants, the powders were pre-treated with helium (50 $cm^3$ $min^{-1}$) at 150 °C for 1 h. After cooling to ambient temperature, TPR experiments were carried out in 10 vol.% $H_2$/Ar (30 $cm^3$ $min^{-1}$) increasing the temperature from room temperature to 600 °C with a heating ramp of 10 °C $min^{-1}$, by a temperature programmable controller. The water produced in the reduction was eliminated using an isopropanol–liquid $N_2$ trap. The hydrogen consumption was calibrated versus CuO and recorded by using as detector a TCD mounted in a GC Shimazdu14-B.

X-ray diffraction (XRD) patterns were obtained with a Philips X'pert PRO apparatus using Cu $K\alpha_1$ radiation ($\lambda = 0.1540$ nm) with a Ge (1 1 1) monochromator working at 45 kV and 40 mA. All the measurements were made with a step size of 0.0167° in 30 min. High resolution patterns were registered in order to apply the Rietveld method to estimate the average crystallite size, using the same step

size but with a total acquisition time of 4 h. The X'pert High Score Plus software was applied for data treatment and calculations, with the standard inner algorithms using pseudo Voigt type curves.

The Raman spectra were obtained using a BRUKER RAM II Raman spectrometer with a Ge detector and the 1064 nm excitation line of Nd-YAG laser. The data were collected by keeping the power at 30 mW, a standard spectral resolution of 4 $cm^{-1}$ and 2000 accumulations for spectrum. The temperature operation was the $N_2$ liquid temperature. The sample powders were pressed into a small disc and then mounted on the analytic chamber. The Raman scattering measurements were carried out in the 200–800 $cm^{-1}$ spectral region.

X-ray photoelectron spectra (XPS) were collected using a Physical Electronics PHI 5700 spectrometer with non-monochromatic Mg Kα radiation (300 W, 15 kV, 1253.6 eV) for the analysis of the core level signals of C 1*s* O 1*s*, Ce 3*d* and Cu 2*p* and with a multichannel detector. Spectra of powdered samples were recorded with the constant pass energy values at 29.35 eV, using a 720 μm diameter analysis area. During data processing of the XPS spectra, binding energy values were referenced to the C 1*s* peak (284.8 eV) from the adventitious contamination layer. The PHI ACCESS ESCA-V6.F software package was used for acquisition and data analysis. A Shirley-type background was subtracted from the signals. Recorded spectra were always fitted using Gauss–Lorentz curves, in order to determine the binding energy of the different element core levels more accurately. The error in BE was estimated to be ca. 0.1 eV. Short acquisition times of 10 min were used to examine Cu 2*p* and Ce 3*d* regions in order to avoid, as much as possible, photoreduction of $Cu^{2+}$ species. Nevertheless, a $Cu^{2+}$ reduction in high vacuum during the analysis cannot be excluded [35].

## 3. Results and discussion

### 3.1. $N_2$ adsorption–desorption

The porous nature of the prepared materials was evaluated by $N_2$ physisorption at −196 °C and the textural properties are presented in Table 1. The bare $CeO_2$ support shows an isotherm of type II with a thin hysteresis loop of type H3, according to the IUPAC classification, exhibiting a relatively low BET specific surface area ($S_{BET}$) (19 $m^2\ g^{-1}$). Upon addition of CuO by impregnation and subsequent calcination, the cumulative pore volume ($V_p$) remains almost constant for all the impregnated samples, while the specific surface area and the pore diameter slightly decrease as a function of the Cu content, indicating that the pores have been partially plugged.

### 3.2. HRTEM microscopy

High-Resolution Transmission Electron Microscopy (HRTEM) images of all the *x*CUCE catalysts are shown in Fig. 1.

The HRTEM image of Fig. 1A (catalyst 3CUCE) exhibits aggregated monocrystalline nanoparticles of ceria, whose size ranges from 7 to 14 nm. The micrograph of a CuO crystallite shows that the particle, of about 7 nm, is superimposed to a $CeO_2$ particle, and the lattice fringes of the two particles present the same orientation. We found this phenomenon widespread on the sample, making us hypothesize that CuO crystallites grew using ceria nanoparticles as a lattice substrate.

Also 6CUCE and 12CUCE samples show the presence of aggregated monocrystalline nanoparticles, whose size ranges from 7 to 14 nm. As to the catalysts 6CUCE (Fig. 1B), CuO crystallite size is about 12 nm and some nanoparticle aggregates of ceria seem to be coated with a nearly uniform amorphous layer (thickness about 5 nm) of CuO encapsulating the aggregates. Sample 12CUCE (Fig. 1C) exhibits some big amorphous particles of copper oxide of 20–30 nm in size, superimposed on some $CeO_2$ crystallites and, similarly to the 6CUCE sample, some ceria particles coated with an amorphous layer of CuO.

### 3.3. $H_2$-TPR

Fig. 2 shows the TPR profiles registered for the bare support and the fresh catalysts. The reduction signal of the nanocrystalline $CeO_2$ sample is formed by two good differentiated peaks. The low temperature peak with a maximum at ∼490 °C is assigned to the reduction of superficial ceria particles, that accounts for a limited surface shell reduction of cerium atoms from +4 to +3 oxidation state: this can be related to a surface reaction probably forming oxygen vacancies [36,37]. The peak at higher temperature corresponding to the reduction of ceria bulk starts at ∼600 °C, but the total reduction of the support to $Ce_2O_3$ cannot occur under the present operating conditions because it usually requires higher temperatures [38,39]. According to the literature, $CeO_2$ is reduced by $H_2$ at temperatures higher than 350 °C. Therefore, peaks in 150–250 °C range can be associated to the reduction of oxidized copper species [40–44]. The TPR profiles of all the catalysts show three reduction peaks (see inset of Fig. 2) and this multiple-step reduction profile has been attributed to the existence of different copper species in the sample. The first maximum (named peak α) appears centered at ∼150 °C. This peak can be associated to the presence of the most easily reducible CuO species, highly dispersed on the surface of nanocrystalline $CeO_2$ and interacting strongly with ceria. At 160–200 °C (peak β) larger CuO particles (even though still in a high dispersion state) become reduced. Finally, the peak centered at ∼220 °C (peak γ) has been assigned to the reduction of bulk CuO. Usually, peaks α and β are related with highly dispersed CuO entities strongly interacting with ceria [45–50], often escaping the XRD detection. The increment of Cu loading seems to cause a certain shift of the reduction peaks toward higher temperatures, indicating increasing difficulty of the $CeO_2$ support in promoting the reduction of copper oxide entities. In any case, copper–cerium interaction is evidenced by the fact that the three reduction peaks are located at temperatures lower than the reduction temperature of pure CuO [12,13] and can be associated to the reduction of oxidized copper species [41–44,46].

Table 2 resumes the results obtained by the deconvolution of the $H_2$-TPR curves to estimate the dispersion degree of copper oxide on the surface of the prepared samples. All the profiles have been

**Table 1**
Textural and structural parameters of the prepared samples.

| Sample | $S_{BET}$ ($m^2\ g^{-1}$)[a] | $V_p$ ($cm^3\ g^{-1}$)[a] | $d_p$ (nm)[a] | Crystalline phases detected[b] | CuO Particle size (nm)[b] | $CeO_2$ Particle size (nm)[b] | $CeO_2$ Strain (%)[b] | $CeO_2$ Lattice Parameter (a/Å)[b] |
|---|---|---|---|---|---|---|---|---|
| $CeO_2$ | 19 | 0.06 | 17.3 | Cerianite | - | 8.5 | 0.2 | 5.412 |
| 3CUCE | 18 | 0.04 | 12.5 | Cerianite tenorite | Not Detectable | 9.9 | 0.2 | 5.412 |
| 6CUCE | 18 | 0.04 | 12.2 | Cerianite, tenorite | 10.7 | 9.9 | 0.2 | 5.412 |
| 12CUCE | 15 | 0.04 | 10.1 | Cerianite, tenorite | 21.9 | 9.8 | 0.2 | 5.412 |

[a] $N_2$ adsorption–desorption data.
[b] Rietveld data.

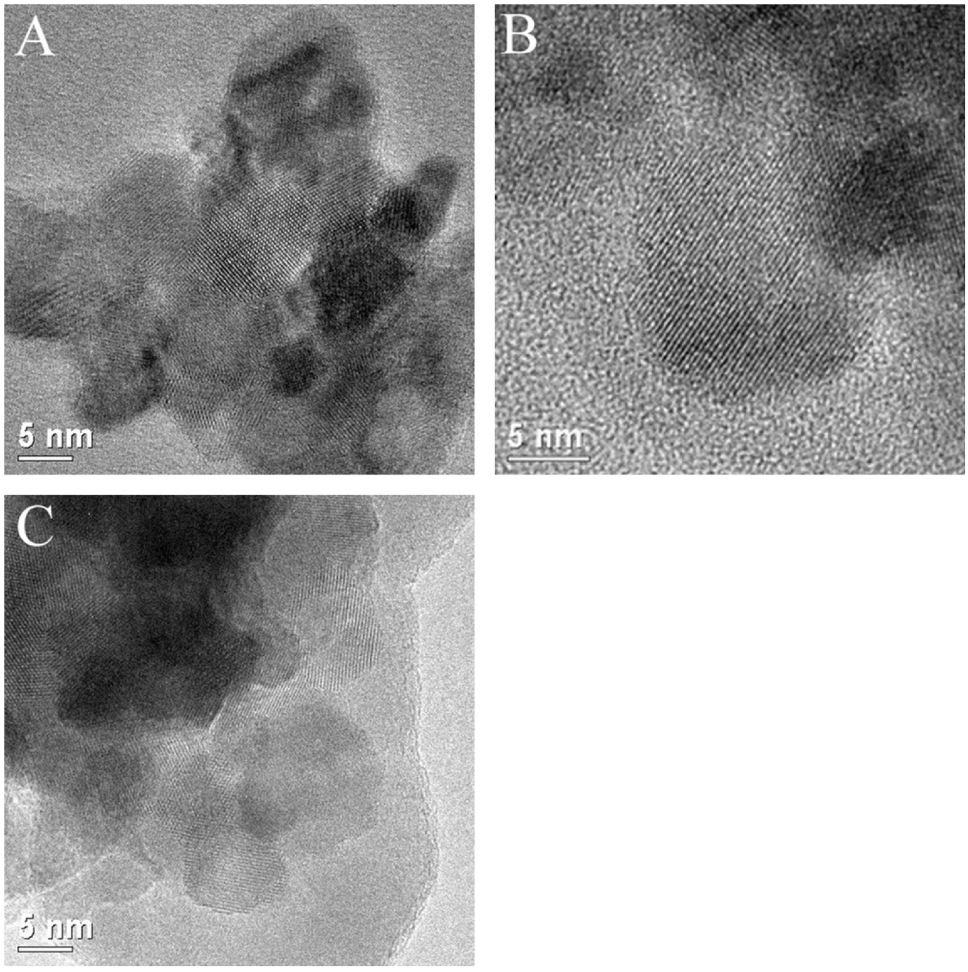


**Fig. 1.** HRTEM micrographs of the *x*CUCE catalysts. (A) 3CUCE; (B) 6CUCE and (C) 12CUCE.

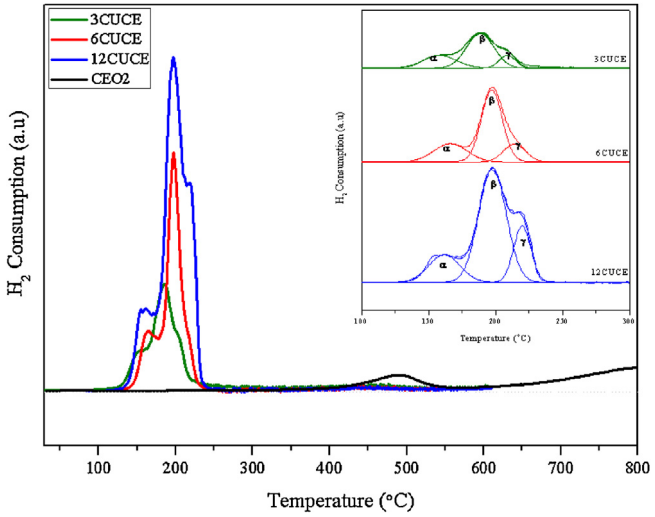


**Fig. 2.** $H_2$-TPR profiles of the bare support and the three CuO-$CeO_2$ catalysts. In the inset the deconvolution of the profiles in the range 100–300 °C.

resolved in three overlapping contributions. The sum of area of the peaks α and β, related to the presence of highly reducible copper species, decreases (from 86.6% to 80.6%) with increasing the amount of copper; while the area of peak γ, due to the presence of bulk CuO, increases (from 13.4% to 19.4%), as expected.

Quantitative analysis of $H_2$ consumed for reduction of copper oxide-ceria systems in the 100–300 °C temperature range are shown in Table 2. Total $H_2$ consumption, that increases with the copper amount in the samples, is higher than the stoichiometric amount required to reduce all the copper of the catalysts from $Cu^{2+}$ to $Cu^0$ and was calculated from the integration of the three superimposed peaks. The theoretical consumption of $H_2$ in function of wt.% of Cu for total reduction of CuO is also included. There is a large discrepancy between theoretical and experimental values. The molar ratio $H_2$/Cu indicates that the $H_2$ consumption of all the catalysts is higher than the theoretical amount necessary for the complete reduction of copper oxide present in the samples. Caputo et al. [46] observed a continuous rise in the global $H_2$ consumption related to reduction peaks at low temperature (around 200 °C) as the copper load increases. However, this exceeded the ideal $H_2$ consumption necessary for the complete $Cu^{2+} \rightarrow Cu^0$ reduction,

**Table 2**
$H_2$-TPR results.

| Sample | Peak α (%) | Peak β (%) | Peak γ (%) | α + β | (α + β)/γ | $H_2$ uptake theoretical (μmol $g^{-1}$) | $H_2$ uptake measured (μmol $g^{-1}$) | $H_2$/Cu |
|---|---|---|---|---|---|---|---|---|
| 3CUCE | 26.2 | 60.4 | 13.4 | 86.6 | 6.5 | 377 | 552 | 1.46 |
| 6CUCE | 24.6 | 59.3 | 16.1 | 83.9 | 5.2 | 755 | 907 | 1.20 |
| 12CUCE | 17.4 | 63.2 | 19.4 | 80.6 | 4.2 | 1510 | 1720 | 1.14 |

suggesting that some $CeO_2$ reduction must occur at low temperatures [51]. On the other hand, the presence of hydrogen spill over on the support in a wide temperature range cannot be discarded [38,47].

### 3.4. CO-PROX catalytic activity

The catalytic activity of the synthesized solids was evaluated in the CO-PROX and the results of the experiment, carried out in the 40–190 °C temperature range with a synthetic reformate gas (1.2% CO, 1.2% $O_2$, 50.0% $H_2$, He), are represented in Fig. 3A and B. It is well known that hydrogen molecules chemisorbed on copper species are dissociated and split over to the surface of support, to form hydroxyl groups which can accelerate the oxidation of CO [48]. For this reason at lower temperatures, mainly oxidation of CO occurs due to its high heat of adsorption than hydrogen, and conversion of CO increases rapidly with the temperature, until it reaches a maximum. For the investigated catalysts, the CO conversion increases with the temperature reaching 100% at 90 °C for the 6CUCE sample and at 115 °C for 3CUCE and 12CUCE. At higher temperatures (above 140 °C), CO conversion starts decreasing, as hydrogen is being more easily oxidized. The selectivity to $CO_2$ is 100% in the 40–80 °C range and, considering the reaction stoichiometry, the oxygen excess factor used and the CO conversion values, the $O_2$ consumption can be exclusively attributable to oxidation of CO to $CO_2$. The effect of the oxygen excess is an important factor in the CO preferential oxidation. It is known that CO conversion increases as the oxygen partial pressure in the feed increases and, generally, a parallel decrease in the $CO_2$ selectivity is observed. According to the literature, the oxygen factor $\lambda = 2$ is the most used ratio and this value was selected to compare the catalytic data registered with the majority of results described in the literature [49,50].

The 6CUCE sample is the most active catalyst at the lowest studied temperatures, while 3CUCE and 12CUCE samples are quite less active in the range 40–115 °C, showing a superimposable reaction profile. For example, at 90 °C, a quite usual PEM Fuel Cells operating temperature, the 6CUCE sample shows a total CO conversion, while that of the 3CUCE and 12CUCE samples is about 75%.

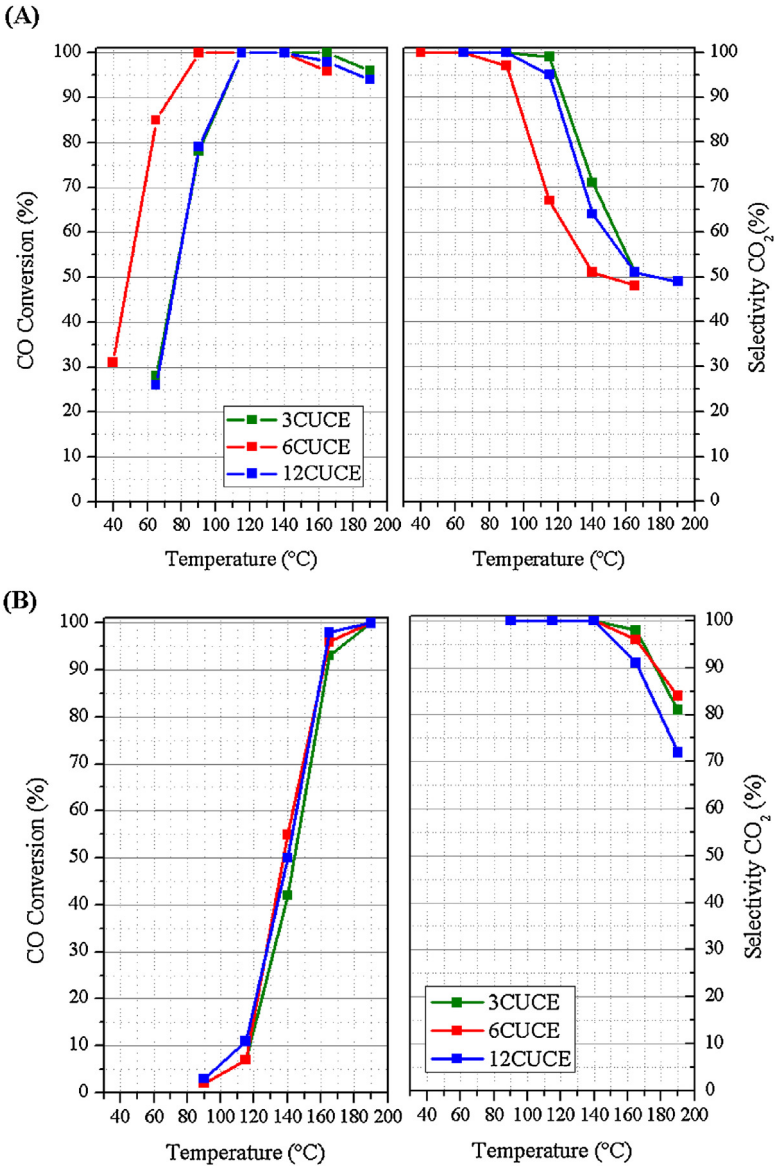


**Fig. 3.** (A) CO conversion and selectivity toward $CO_2$ as function of the temperature over the *x*CUCE. Operating conditions: GHSV = 22,000 $h^{-1}$, $\lambda = 2$, 1.25% CO, 1.25%$O_2$, 50% $H_2$, He balance (vol.%). (B) CO conversion and selectivity toward $CO_2$ as function of the temperature also in the presence of $CO_2$ and $H_2O$. Operating conditions: GHSV = 22,000 $h^{-1}$, $\lambda = 2$, 1.25% CO, 1.25%$O_2$, 50% $H_2$, 15% $CO_2$, 10% $H_2O$, He balance (vol.%).

The effect of time on stream was studied over the sample 6CUCE (not shown), using the following operating conditions: GHSV = 22,000 $hL^{-1}$, λ = 2, feed stream: 1.25% CO, 1.25%$O_2$, 50% $H_2$, He balance (%vol). The reaction was monitored for 36 h maintaining the temperature constant at 115 °C. The CO conversion decreased from 100% to 97.5% within the first 4 h, then it remained stable for the further 32 h of operation. The selectivity to $CO_2$ was 75% during all the experiment.

High activity and selectivity are decisive for a real CO-PROX application, but there are other important factors, which have to be considered as well, e.g. the effects arising from a more realistic composition of the reaction gas mixture. Since a catalyst of selective oxidation of CO must be resistant to $CO_2$ and $H_2O$, all the samples were tested in $H_2$-rich feed also in the presence of both 15 vol.% $CO_2$ and 10 vol.% $H_2O$.

Catalytic tests have demonstrated deactivating effects of both $CO_2$ and $H_2O$ molecules on the CO-PROX performance of the tested catalysts. Mariño et al. [51] proposed that a decreasing in CO conversion and $CO_2$ selectivity with increasing $CO_2$ content in the stream up to 15% could be related to competitive adsorption of $CO_2$ on the active copper sites and/or inhibition of oxygen mobility caused by the formation of carbonates on the ceria support. Gamarra et al. [50] related the diminution of activity to modifications of interfacial sites upon formation of specific carbonates, due to the presence of $CO_2$ in the reactant stream, and a blocking effect induced by the presence of adsorbed molecular $H_2O$, limiting the access of the reactant molecules to the sample surface. When $CO_2$ and $H_2O$ were added to the gas stream, the $T_{50}$ value (temperature at which the CO conversion is 50%) of the three catalysts shifted toward much higher temperatures (Fig. 3) 6CUCE sample exhibits a shift of the $T_{50}$ from 50 °C to about 130 °C, while the selectivity to $CO_2$ still remains 100%. Nevertheless, despite these expected deactivation phenomena, a CO conversion value higher than 90% and a $CO_2$ selectivity of about 90% can be achieved for all the samples at 160 °C.

These results point out that, for $CuO/CeO_2$ systems in the CO-PROX reaction, a high catalyst specific surface area value seems to be not a critical factor to achieve a good catalytic performance. In this sense, most relevant aspects of CO-PROX activity appear to be related to the competition between CO and $H_2$ oxidation activities, which basically determine the selectivity for the process. Concerning the former (CO oxidation), there is general consensus that it can be related to the presence of reduced states of copper (in the form of $Cu^+$) at copper oxide–ceria interfacial positions. The interfacial character of such sites basically determines that well dispersed CuO entities contribute most to the activity, although active interfaces could be obtained either in direct ($CuO/CeO_2$) or inverse ($CeO_2/CuO$) configurations, the latter having large size CuO particles [52,53]. Such interfacial reduced states of copper could either be present in the initial catalyst [16] or (when starting with fully oxidized catalysts) are formed during the course of the reaction as a consequence of redox interaction with the reactant mixture [21]. In this sense, further than the general specific surface area value, the interfacial area and/or its physicochemical characteristics appear to be most relevant to explain CO oxidation activity achieved by the catalysts. In the latter sense, changes in the type of interacting oxides surfaces appear also of relevancy, as reported in studies in which copper/ceria samples with different specific faces exposed in the $CeO_2$ component were prepared [52,53]. More doubts exist with respect to the selectivity (i.e. basically related to oxygen selectively reacting with CO during competition with $H_2$) achieved in each case. It has been proposed that selectivity could originate from the fact that active sites for CO oxidation could be different than those for $H_2$ oxidation, the latter being related to reduced copper sites formed on top of the dispersed CuO particles, subjected to a lower degree of interaction with the underlying $CeO_2$ support [21]. This hypothesis appears also in agreement with the fact that kinetics for CO oxidation does not appear much affected by the presence of $H_2$ [49]. However, it has been recently pointed out that the origin of the selectivity could be related to the strength of the adsorption of CO (forming chemisorbed carbonyl species), $H_2$ oxidation starting when sites on reduced copper become free as a consequence of CO desorption, therefore both reactions (CO and $H_2$ oxidation) basically sharing the same active sites [54]. In any case, the role of the support appears to be related to promotion of the reduction of copper oxide (thus leading to generation of active reduced copper species), while its specific role during the reaction remains unknown although most likely active sites require also a certain level of interfacial support reduction [21].

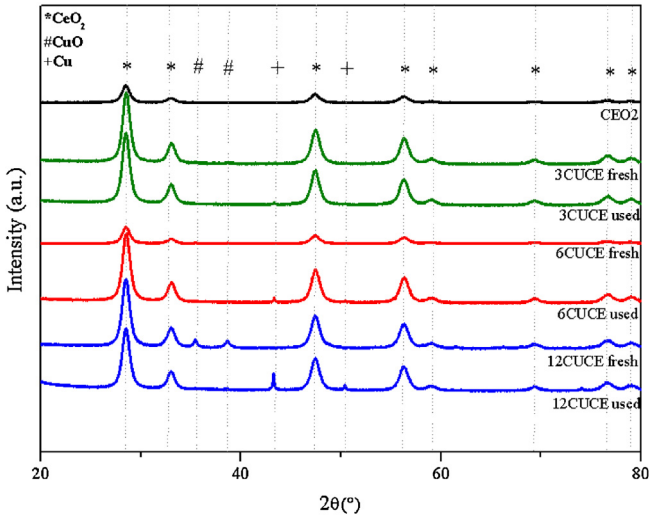


**Fig. 4.** XRD patterns of the bare support and the catalysts before and after one cycle of CO-PROX activity.

### 3.5. X-ray diffraction

Fig. 4 shows the XRD patterns of the three 3CUCE, 6CUCE and 12CUCE catalysts before and after one cycle of CO-PROX catalytic reaction and the bare $CeO_2$ as comparison. All the samples show the characteristic diffraction peaks of $CeO_2$ at $2\theta$ = 28.5, 33.4, 47.5 and 56.5°, that can be assigned to the cerianite cubic phase (ICDS 01-081-0792).

Reflection lines corresponding to copper oxide as tenorite phase (peaks at $2\theta$ = 35.5 and 38.9°, ICDS 01-089-2529) are found in the fresh form of two of the three examined catalysts, 6CUCE and 12CUCE, increasing their intensity, as expected, with the increasing amount of copper. This is typical for samples prepared by impregnation and subsequent calcination, because this procedure can lead to a partial segregation of copper in the form of CuO [10]. The mean size of copper oxide particles was calculated from the half-width of the main peak at $2\theta$ = 35.5°, according to the Rietveld method and resulted: 10.7 nm for 6CUCE and 21.9 nm for 12CUCE (Table 1). It must be noted that this does not discard the presence of dispersed copper entities escaping detection by XRD technique. As to the sample 3CUCE, no copper-containing phases are discerned in the pattern, most probably due to high dispersion of CuO nanoparticles with too small particle sizes to be identified by the conventional XRD method. The average crystallite size of ceria has been estimated by Rietveld methodology [55,56] and summarized in Table 1. After the addition of copper oxide, the crystallite size of cerianite slightly increases and its value changes from 9.5 to 9.9 nm for all the catalysts. On the contrary, the cell parameter of ceria does not decrease with the increment of the Cu content and remains

constant at 5.412 Å. This suggests that no appreciable fraction of copper has been incorporated into the ceria lattice and the majority of copper must be present either in the form of large segregated CuO particles, as detected by XRD measurements, or as dispersed entities on the surface of ceria nanocrystals, as shown by HRTEM micrographs. It should be considered in this sense that substitutional $Cu^{2+}$ incorporation into the ceria lattice could lead to a decrease of the lattice parameter, as a consequence of the lower ionic radius of $Cu^{2+}$ with respect to that of $Ce^{4+}$ although this is still under debate, as discussed elsewhere [9]. The strain in the $CeO_2$ lattice does not change with the addition of CuO (Table 1), leading us to believe that the incorporation into the lattice has not occurred. Raman results described below could determine whether part of the copper loaded is incorporated into the ceria lattice [9]. After one cycle of CO-PROX reaction, reflection lines associated to metallic Cu at $2\theta = 43.5$ and 50.4° appear in the catalysts 6CUCE and 12CUCE, with intensity increasing with the amount of copper, indicating the reduction of some of the copper during the reaction in the presence of excess hydrogen, in agreement with previous investigation on other Cu-Ce based catalysts [57,58]. On the other hand, a small shift to lower angles of the diffraction peaks and the increase in the lattice parameters of the cerianite phase observed in the used samples suggest a partial reduction of ceria.

### 3.6. Raman spectroscopy

Information about oxygen vacancies in the catalysts surface or sub-surface levels can be obtained by Raman spectroscopy. Fig. 5A shows the Raman spectra of the pure support ceria and catalysts *x*CUCE, as well as of pure CuO as a reference. In agreement to the literature [59] three Raman bands are observed in crystalline pure CuO sample centred at 296, 345 and 629 $cm^{-1}$.

A band at approximately 468 $cm^{-1}$ is observed for all the catalysts and the support $CeO_2$. This absorption band is ascribed to the Raman active $F_{2g}$ mode of $CeO_2$ cubic lattice, which can be viewed as a symmetric breathing mode of the oxygen atoms around cerium ions [60,61]. This band is higher in the 6CUCE than in both 3CUCE and 12CUCE catalyst where it becomes broader, while a small red shift with respect to that of pure ceria is also detected and this can be related to a small residual addition of Cu in the lattice of ceria [10], most likely at positions close to the surface. It is known that the cerianite structure tolerates a relatively high level of atomic disorder upon the incorporation of metal cations into the ceria lattice. The crystal lattice is then forced to compensate the excess of negative charge upon incorporation of the heterocation with positive charge lower than that of cerium cations ($Cu^{2+}$ in this case). Intrinsic oxygen vacancies are generated by this process upon addition of $Cu^{2+}$ dopant cations for charge balance [62,63]. After catalysis (Fig. 5B), the signal at 468 $cm^{-1}$ of the samples 6CUCE and 12CUCE decreases in intensity, while no variations in the Raman signal are detected for the sample 3CUCE. The explanation to the change in the intensity of the signal could be related to the presence of metallic copper, because it usually produces a loss of intensity of the Raman shift caused by the absorption of the excitation wave. The diffractograms of the used catalysts, excepting for the sample with a 3 wt.% Cu, show peaks of metallic copper (Fig. 4). Another explanation could be a considerable or total reduction of the ceria support, but this hypothesis is ruled out by XRD results. Furthermore, the catalytic reaction takes place at lower temperatures than the onset reduction of ceria, as explained in the $H_2$-TPR paragraph. The spectra for all catalysts (see Fig. 5A) show the absence of peaks at 296 and 345 $cm^{-1}$ assigned to CuO. The shift to about 629 $cm^{-1}$, usually related to the presence of oxygen vacancies is not perceptible. As previously observed by XRD measurements, this could suggest that CuO is highly dispersed on the surface of the ceria grains and the ceria lattice has not been modified by the addition of copper oxide.

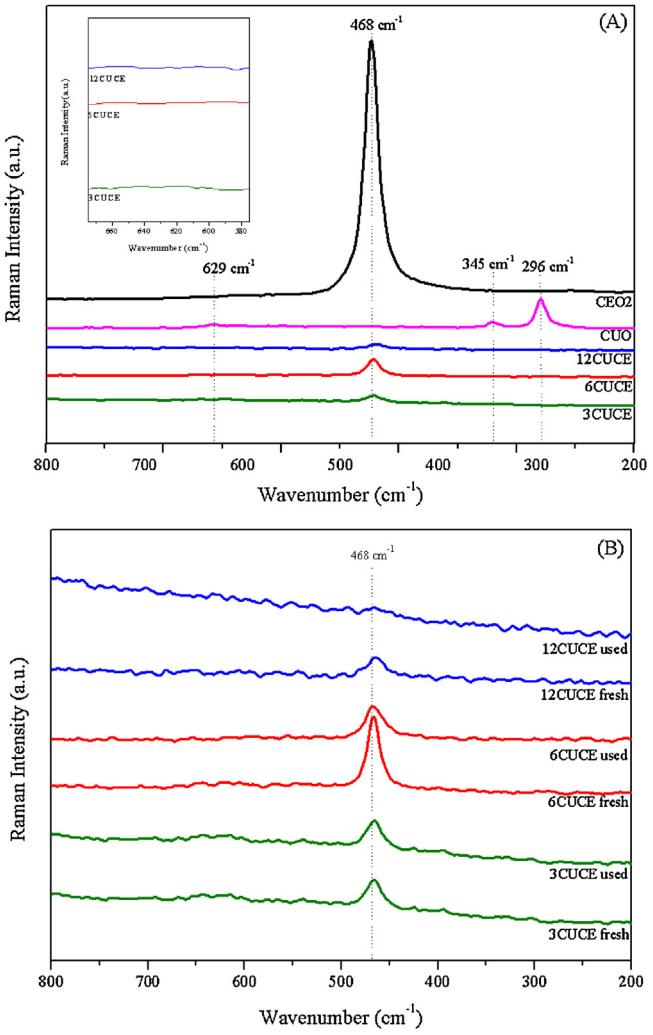


**Fig. 5.** (A) Raman shifts of the bare ceria support and the catalysts referred to pure $CuO_2$. In the inset, a magnification in the range 670–570 $cm^{-1}$. (B) Comparison of Raman shifts of catalysts before and after one cycle of CO-PROX activity.

### 3.7. XPS spectroscopy

The composition and the oxidation state of the elements at the surface of the support and catalysts have been studied by XPS. Fig. 6 resumes the spectra registered in O 1*s*, Cu 2*p*, CuLMM and Ce 3*d* regions and Table 3 resumes the surface chemical composition of the catalysts determined by XPS.

All the spectra registered were referred to signal C 1*s* 284.8 eV corresponding to adventitious carbon. Two overlapped peaks at

**Table 3**
Chemical composition of the surface (in atomic concentration %) and Cu/Ce and Cu/(Cu + Ce) ratios for the studied catalysts determined by XPS.

| Sample | %C | %O | %Cu | %Ce | Cu/Ce | Cu/(Cu + Ce) |
|---|---|---|---|---|---|---|
| $CeO_2$ | 38.8 | 44.8 | - | 16.5 | - | - |
| 3CUCE fresh | 28.7 | 48.9 | 2.8 | 19.5 | 0.14 | 0.13 |
| 3CUCE used | 43.1 | 39.9 | 2.6 | 14.4 | 0.18 | 0.15 |
| 6CUCE fresh | 30.3 | 48.1 | 7.8 | 13.8 | 0.57 | 0.36 |
| 6CUCE used | 34.6 | 39.2 | 13.2 | 12.9 | 1.02 | 0.51 |
| 12CUCE fresh | 25.1 | 47.6 | 14.8 | 12.6 | 1.17 | 0.54 |
| 12CUCE used | 31.8 | 43.1 | 6.35 | 18.7 | 2.95 | 0.75 |

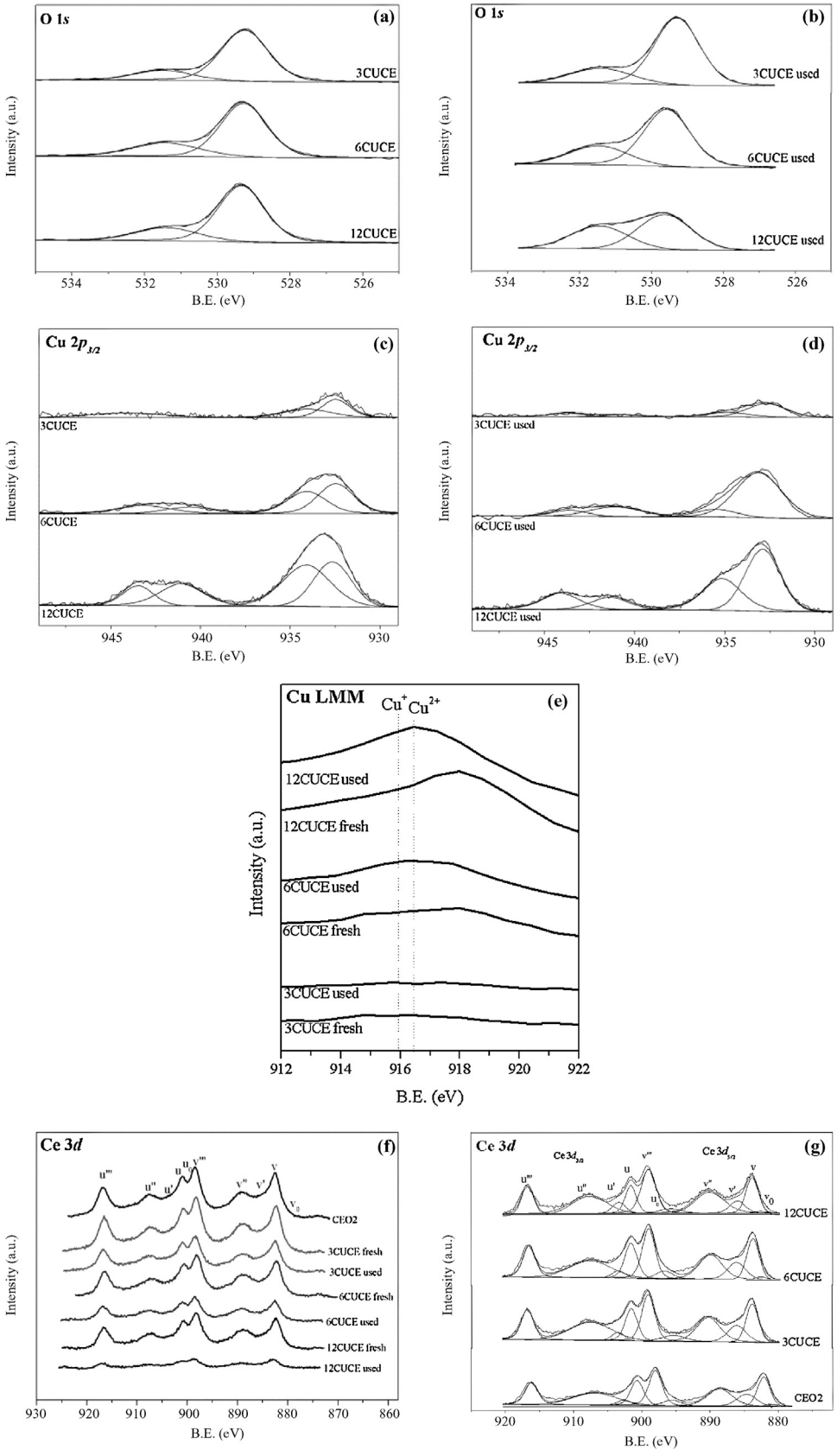


**Fig. 6.** XPS spectra of the studied catalysts. (a) O 1*s* fresh catalysts; (b) O 1*s* used catalysts; (c) Cu $2p_{3/2}$ fresh catalysts; (d) Cu $2p_{3/2}$ used catalysts; (e) Cu LMM; (f) Ce 3*d* fresh catalysts; (g) Ce 3*d* region of the support and the catalysts (fresh and used).

**Table 4**
Binding energies and redox parameters of the support and the catalysts, before and after catalytic reaction, determined by XPS.

| Sample | B.E. (eV) | Cu $2p_{3/2}$ (eV) | $Cu_{red}$/CuO | $I_{sat}/I_{pp}$ | $Ce^{3+}/Ce^{4+}$ |
|---|---|---|---|---|---|
| $CeO_2$ | 529.3 (78.3%)531.4 (21.7%) | - | - | - | 0.46 |
| 3CUCE fresh | 529.2 (80.7%)531.5 (19.3%) | 932.5 (81.5%)934.1 (18.5%) | 0.82 | 0.36 | 0.42 |
| 3CUCE used | 529.3 (74%) 531.5 (26%) | 932.7 (69.7%)934.5 (30.2%) | 0.93 | 0.31 | 0.42 |
| 6CUCE fresh | 529.3 (72.9%)531.4 (27.1%) | 932.8 (81.2%)934.8 (18.1%) | 0.82 | 0.36 | 0.32 |
| 6CUCE used | 529.6 (68%) 531.5 (32%) | 933.1 (86.7%)935.4 (13.3%) | 0.87 | 0.31 | 0.40 |
| 12CUCE fresh | 529.4 (76.3%)531.4 (23.7%) | 932.7 (44.5%)934.9 (55.5%) | 0.44 | 0.47 | 0.15 |
| 12CUCE used | 529.6 (56.7%)531.4 (43.3%) | 932.8 (60.7%)935.1 (39.3%) | 0.61 | 0.35 | 0.39 |

284.8 eV and at 289 eV are present in all the spectra of C 1*s* region, which evidences the presence of carbonates on the surface of the samples before and after CO-PROX reaction. The O 1*s* core level signal shows two contributions, one very intense at ~529 eV assigned to metallic oxides and other at 531.5 eV due to the presence of hydroxyl or carbonates at the surface of the samples (Fig. 6a). After reaction, the contribution at 531.5 eV experiments an increase for all the catalysts, being important for 12CUCE catalyst (Fig. 6b). Nevertheless the contribution of the signal at 531.5 eV increases in a lower percentage amount in the sample 6CUCE. It may suggest the presence of a lower amount of carbonates at the surface of this catalyst after one cycle of CO-PROX reaction.

To avoid photoreduction of Ce and Cu, short irradiation times have been used [43]. In Cu $2p_{3/2}$ region (Fig. 6c and d), the peak with a maximum at ~933.1 eV and the shake-up satellite at ~942.1 eV indicate the presence of $Cu^{2+}$. The main peak can be decomposed in two contributions: one at ~932.8 eV assigned to $Cu^{1+}$ and other one at higher binding energy, about ~934.8 eV, corresponding to $Cu^{2+}$ species. Therefore, it is supposed that copper is present on the catalysts under study as CuO and $Cu_2O$ [64,65]. This assumption was corroborated with the study of le line Auger Cu LMM. In these spectra (Fig. 6e) it is possible to distinguish between a peak at 916 eV that corresponds to $Cu^{+}$ and anther one at ~918 eV of $Cu^{2+}$ that is in concordance with the $H_2$-TPR results and suggested the presence of different copper species. After catalysis, the $Cu_{red}$/CuO atomic ratio increases from 0.82 to 0.87 for 6CUCE and from 0.82 to 0.93 for 3CUCE. The main peak of Cu $2p_{3/2}$ is centered ~935 eV and the reduction of the $I_{sat}/I_{pp}$ ratio is due in to the majority presence of $Cu^{1+}$ on the surface of the used catalysts.

The Ce 3*d* spectra of the 6CUCE fresh and after catalytic reaction are illustrated in Fig. 6f and g.

The complexity of the spectra is a consequence of the hybridization between the Ce 4*f* levels and the O 2*p* states [66]. The spectra can be decomposed in ten contributions: v, u (Ce $3d^9$ $4f^2$ O $2p^4$) and v″, u″ (Ce $3d^9$ $4f^1$ O $2p^5$); v‴, u‴ (final state of Ce $3d^9$ $4f^0$ O $2p^6$) assigned to Ce(IV); $v_0$,$u_0$ (Ce $3d^9$ $4f^2$ O $2p^5$) and v′, u′ (Ce $3d^9$ $4f^1$ O $2p^6$) assigned to Ce(III) [67,68].

The surface atomic ratios Cu/Ce (Table 3) increase proportionally with the amount of CuO. The Cu/Ce ratio ranges from 0.14 for 3CUCE to 1.17 for 12CUCE. This is an indication of loss of dispersion of CuO on the surface of the supports, as previously suggested.

In Table 4 the $Ce^{3+}/Ce^{4+}$ values are included. The support has an atomic ratio of 0.46. This relation decreases in the fresh catalysts with the wt.% Cu content, from 0.42 for the sample 3CUCE to 0.15 for 12CUCE. The variation in the $Ce^{3+}/Ce^{4+}$ values in function of the amount of CuO evidences the strong interaction existing between both metal oxides.

As expected the $Ce^{3+}/Ce^{4+}$ atomic ratio increases after catalysis indicating a partial reduction of $Ce^{4+}$ at the sample surfaces.

Studying the redox mechanism for CO oxidation in CuO/$CeO_2$ systems [69–70], it has been suggested the existence of a first reaction step involving reduction with CO (and concomitant $CO_2$ evolution), initiated by $Ce^{4+}$ and $Cu^{2+}$ species and leading to the generation of mainly $Cu^{+}$ and $Ce^{3+}$ species at the interface between copper oxide and $CeO_2$ support. Sample 6CUCE exhibits a lower $Ce^{3+}/Ce^{4+}$ atomic ratio before catalysis than 3CUCE, thus, despite the lower percentage area of highly dispersed CuO species exhibited by this catalyst in the $H_2$-TPR analysis, in comparison with the sample 3CUCE, the presence of an overall higher amount of $Ce^{4+}$ species before reaction seems to provide a higher amount of very active sites in the CO oxidation.

Considering all the experimental evidences so far exposed, the highest overall activity displayed by sample 6CUCE can be the consequence of a balance of factors involving not only the dispersion of the copper species but also the presence of the opportune amount of $Ce^{4+}$ that can generate, during the reaction with CO, catalytically active copper sites.

## 4. Conclusions

Nanocrystalline $CeO_2$ with a regular size of 9.5 nm was prepared by a freeze-drying method, and subsequent impregnated with a Cu(II) acetate solution, varying the loading of Cu (3, 6, 12 wt.%). The resulting CuO/$CeO_2$ systems seem to be promising candidate catalysts for the selective removal of CO from $H_2$-rich gas streams, above all the catalyst 6CUCE, that exhibits the highest performance among the three studied samples, reaching a 100% of CO conversion at 90 °C and starting to diminish its performance above 140 °C, maintaining an excellent conversion in the range technologically interesting for the PEMFCs. According to all the results previously exposed, it can be suggested that the good CO-PROX catalytic behavior of these catalysts can be related to the wide dispersion of the copper active sites associated with the high amount of $Ce^{4+}$ species before reaction, notwithstanding the low surface area of the nanocrystalline ceria.

## Acknowledgements

The Spanish authors appreciate the financial support by the project CTQ2012-37925-C03-03 (Ministerio de Economía y Competitividad, Spain), MAT2007-60127 and MAT2010-16007 (Cofinanced by MICINN and FEDER funds) and by the project FQM01661 (Proyecto de Excelencia de la Junta de Andalucía, Spain). JMJ thanks Spanish Government Research Program for grants MAT2007-60127 and MAT2010-16007 and for pre-doctoral fellowship (FPI).

## References

[1] N.Q. Minh, T. Takahashi, Science and Technology of Ceramic Fuel Cells, Elsevier, Amsterdam, 1995, pp. 69–116.
[2] S.C. Singhal, K. Kendall, High Temperature Solid Oxide Fuel Cells, Elsevier, Oxford, 2004.
[3] B. Lindström, L.J. Pettersson, Int. J. Hydrog. Energy 26 (2001) 923–933.
[4] Y. Zhang, H. Liang, X.Y. Gao, Y. Liu, Catal. Comm. 10 (2009) 1432–1436.

[5] J.D. Morse, Int. J. Energy Res. 31 (2007) 576–602.
[6] D.L. Trimm, Appl. Catal. A: Gen. 296 (2005) 1–11.
[7] G. Avgouropoulos, T. Ioannides, H. Matralis, Appl. Catal. B 56 (2005) 87–93.
[8] G. Avgouropoulos, T. Ioannides, Appl. Catal. B 67 (2006) 1–11.
[9] D. Gamarra, G. Munuera, A.B. Hungría, M. Fernández-García, J.C. Conesa, P.A. Midgley, X.Q. Wang, J.C. Hanson, J.A. Rodríguez, A. Martínez-Arias, J. Phys. Chem. C 111 (2007) 11026–11038.
[10] E. Moretti, M. Lenarda, L. Storaro, A. Talon, R. Frattini, S. Polizzi, E. Rodríguez-Castellón, A. Jiménez-López, Appl. Catal. B 72 (2007) 149–156.
[11] E. Moretti, M. Lenarda, L. Storaro, A. Talon, T. Montanari, G. Busca, E. Rodríguez-Castellón, A. Jiménez-López, M. Turco, G. Bagnasco, R. Frattini, App. Catal. A 335 (2008) 46–55.
[12] E. Moretti, L. Storaro, A. Talon, R. Moreno-Tost, E. Rodríguez-Castellón, A. Jiménez-López, M. Lenarda, Catal. Lett. 129 (2009) 323–330.
[13] D. Gamarra, A. Hornés, Zs. Koppàny, Z. Schay, G. Munuera, J. Soria, A. Martínez-Arias, J. Power Sources 169 (2007) 110–116.
[14] D. Gamarra, A.L. Cámara, M. Monte, S.B. Rasmussen, L.E. Chinchilla, A.B. Hungría, G. Munuera, N. Gyorffy, Z. Schay, V.C. Corberán, J.C. Conesa, A. Martínez-Arias, Appl. Catal. B 130–131 (2013) 224–238.
[15] W. Liu, A.F. Sarofim, M. Flytzani-Stephanopoulos, Chem. Eng. Sci. 49 (1995) 4871–4888.
[16] B. Skårman, D. Grandjean, R.E. Benfield, A. Hinz, A. Andersson, L.R. Wallenberg, J. Catal. 211 (2002) 119–133.
[17] A.N. Ilichev, A.A. Firsova, V.N. Korchak, Kinet. Catal. 47 (2006) 585–592.
[18] W. Liu, M. Stephanopoulos, J. Catal. 153 (1995) 304–316.
[19] D. Gamarra, C. Belver, M. Fernández-García, A. Martínez-Arias, J. Am. Chem. Soc. 129 (2007) 12064–12065.
[20] G. Avgouropoulos, T. Ioannides, Ch. Papadopoulou, J. Batista, S. Hocevar, H.K. Matralis, Catal. Today 75 (2002) 157–167.
[21] A. Trovarelli, Catal. Rev. Sci. Eng. 38 (1996) 439–520.
[22] X.C. Zheng, S.P. Wang, S.R. Wang, S.M. Zhang, W.P. Huang, S.H. Wu, Mater. Sci. Eng. C 25 (2005) 516–520.
[23] M. Fernandez-Garcia, A. Martinez-Arias, A. Iglesias-Juez, C. Belver, A.B. Hungria, J.C. Conesa, J. Soria, J. Catal. 194 (2000) 385–392.
[24] A. Martinez-Arias, M. Fernandez-Garcia, A.B. Hungria, A. Iglesias-Juez, O. Galvez, J.A. Anderson, J.C. Conesa, J. Soria, G. Munuera, J. Catal. 214 (2003) 261–272.
[25] A. Martinez-Arias, A.B. Hungria, M. Fernandez-Garcia, J.C. Conesa, G. Munuera, J. Phys. Chem. B 108 (2004) 17983–17991.
[26] A. Martinez-Arias, A.B. Hungria, G. Munuera, D. Gamarra, Appl. Catal. B 65 (2006) 207–216.
[27] Z. Liu, R. Zhou, X. Zheng, J. Nat. Gas Chem. 16 (2007) 167–172.
[28] D. Pérez-Coll, P. Núñez, D. Marrero-López, J.C.C. Abrantes, J.R. Frade, J. Solid State Electrochem. 8 (2004) 644–649.
[29] J.C.C. Abrantes, D. Pérez-Coll, P. Núñez, J.R. Frade, Electrochim. Acta 48 (2003) 2761–2766.
[30] D. Perez-Coll, P. Nunez, J.R. Frade, J.C.C. Abrantes, Electrochim. Acta 48 (2003) 1551–1557.
[31] M.L. Ferrer, R. Esquembre, I. Ortega, C.R. Mateo, F. del Monte, Chem. Mater. 18 (2006) 554–559.
[32] S. Deville, E. Saiz, A.P. Tomsia, Biomaterials 27 (2006) 5480–5489.
[33] S.R. Mukai, H. Nishihara, S. Shichi, H. Tamon, Chem. Mater. 16 (2004) 4987–4991.
[34] S. Deville, E. Saiz, R.K. Nalla, A.P. Tomsia, Science 311 (2006) 515–518.
[35] S. Poulston, P.M. Parlett, P. Stone, M. Bowker, Surf. Interface Anal. 24 (1996) 811–820.
[36] A. Pintar, J. Batista, S. Hočevar, J. Colloid Interface Sci. 285 (2005) 218–231.
[37] Y. Liu, T. Hayakawa, K. Suzuki, S. Hamakawa, T. Tsunoda, T. Ishii, M. Kumagai, Appl. Catal. A 223 (2002) 137–145.
[38] P. Bera, K.R. Priolkar, P.R. Sarode, M.S. Hedge, S. Emura, R. Kumashiro, Chem. Mater. 14 (2002) 3591–3601.
[39] S. Piras, A. Colussi, A. Trovarelli, V. Sergo, J. Llorca, R. Psaro, L. Sordelli, J. Phys. Chem. B 109 (2005) 11110–11118.
[40] M.F. Luo, Y.J. Zhong, X.X. Yuan, X.M. Zheng, Appl. Catal. A 232 (1997) 121–131.
[41] E. Moretti, L. Storaro, A. Talon, M. Lenarda, Catal. Commun. 10 (2009) 522–527.
[42] E. Moretti, L. Storaro, A. Talon, P. Riello, R. Frattini, M. Lenarda, Microporous Mesoporous Mater. 116 (2008) 575–580.
[43] E. Basaldella, E. Tara, G. Aguilar-Armenta, M.E. Patiño-Iglesias, E. Rodríguez-Castellón, J. Sol. Gel Sci. Technol. 37 (2006) 141–146.
[44] J. Papavasiliou, G. Avgouropoulos, T. Ioannides, Appl. Catal. B: Environ. 68 (2007) 226–234.
[45] A. Gurbani, J.L. Ayastuy, M.P. González-Marcos, M.A. Gutiérrez-Ortiz, Int. J. Hydrogen Energy 35 (2010) 11582–11590.
[46] T. Caputo, L. Lisi, R. Pirone, G. Russo, Appl. Catal. A 348 (2008) 42–53.
[47] J.M. Gatica, R.T. Baker, P. Fornasiero, S. Bernal, G. Blanco, J. Kaspar, J. Phys. Chem. B 1004 (2000) 4472–4667.
[48] C. Shengzhou, H. Zou, Z. Liu, W. Lin, Appl. Surf. Sci. 255 (2009) 6963–6967.
[49] H.C. Lee, D.H. Kim, Catal. Today 132 (2008) 109–116.
[50] D. Gamarra, A. Martínez-Arias, J. Catal. 263 (2009) 189–195.
[51] F. Mariño, C. Descorme, D. Duprez, Appl. Catal. B 58 (2005) 175–183.
[52] A.P. Jia, S.Y. Jiang, J.Q. Lu, M.F. Luo, J. Phys. Chem. C 114 (2010) 21605–21610.
[53] K. Zhou, R. Xu, X. Sun, H. Chen, Q. Tian, D. Shen, Y. Li, Catal. Lett. 101 (2005) 169–173.
[54] J. Han, H.J. Kim, S. Yoon, H. Lee, J. Mol. Catal. A 335 (2011) 82–88.
[55] R. Kydd, D. Ferri, P. Hug, J. Scott, W.Y. Teoh, R. Amal, J. Catal. 277 (2011) 41–64.
[56] H.M. Rietveld, J. Appl. Crystallogr. 2 (1969) 65–71.
[57] P.H. Suherman, A. van Riesen, B. O'Connor, D. Li, D. Bolton, H. Fairhurst, Powder Diffr. 17 (2002) 178–185.
[58] E. Moretti, L. Storaro, A. Talon, M. Lenarda, P. Riello, R. Frattini, M.V. Martínez de Yuso, A. Jiménez López, E. Rodríguez Castellón, F. Ternero, A. Caballero, J.P. Holgado, Appl. Catal. B 102 (2011) 627–637.
[59] E. Moretti, M. Lenarda, P. Riello, L. Storaro, A. Talon, R. Frattini, A. Reyes-Carmona, A. Jiménez-López, E. Rodríguez-Castellón, Appl. Catal. B 129 (2013) 556–565.
[60] J.F. Xu, W. Ji, Z.X. Shen, W.S. Li, S.H. Tang, X.R. Ye, D.Z. Jia, X.Q. Xin, J. Raman Spectrosc. 30 (1999) 413–415.
[61] B.M. Reddy, A. Lakshmanan, J. Khan, Phys. Chem. B 108 (2004) 16855–16863.
[62] W. Shan, Z. Feng, Z. Li, W. Shen, C. Li, J. Catal. 228 (2004) 206–217.
[63] J.E. Spanier, R.D. Robinson, F. Zhang, S.W. Chan, I.P. Herman, Phys. Rev. B 64 (2001) 245407.
[64] J.R. McBride, K.C. Hess, B.D. Pointdexter, W.H. Weber, J. Appl. Phys. 76 (1994) 2435–2441.
[65] G. Avgouropoulos, T. Ioannides, Appl. Catal. A 244 (2003) 155–167.
[66] J. Xiaoyuan, L. Liping, C. Yingxu, Z. Xiapming, J. Mol. Catal. A 197 (2003) 193–205.
[67] J.P. Holgado, G. Munuera, J.P. Espinós, A.R. González-Elipe, Appl. Surf. Sci. 158 (2000) 164–171.
[68] F. Zhang, P. Wang, J. Koberstein, S. Khalid, S.W. Chan, Surf. Sci. 563 (2004) 74–82.
[69] X.C. Zheng, S.P. Wang, S.M. Zhang, W.P. Huang, S.H. Wu, Mater. Sci. Eng. 25 (2005) 516–520.
[70] A. Martinez-Arias, M. Fernandez-Garcia, O. Galvez, J.M. Coronado, J.A. Anderson, J.C. Conesa, J. Soria, G. Munuera, J. Catal. 195 (2000) 207–216.